PROCEEDINGS, 50th Workshop on Geothermal Reservoir Engineering
Stanford University, Stanford, California, February 10-12, 2025
SGP-TR-229

Conclusions from the WHOLESCALE Project at the Geothermal Field at San Emidio, Nevada, U.S.

Kurt L. Feigl and Team WHOLESCALE

University of Wisconsin-Madison, 1215 West Dayton St., Madison, WI, 53706 USA

feigl@wisc.edu

Keywords: WHOLESCALE, San Emidio, EGS, GPS, INSAR, FEM, GEOS

ABSTRACT

The WHOLESCALE acronym stands for Water & Hole Observations Leverage Effective Stress Calculations and Lessen Expenses. The goal of the WHOLESCALE project is to simulate the spatial distribution and temporal evolution of stress in the geothermal system at San Emidio in Nevada, United States. To reach this goal, the WHOLESCALE team has developed a methodology to incorporate and interpret data from four methods of measurement into a multi-physics model that couples thermal, hydrological, and mechanical (T-H-M) processes. The WHOLESCALE team includes personnel from two universities, two national laboratories, and one industry partner. The WHOLESCALE team has taken advantage of the perturbations created by changes in pumping operations during planned shutdowns in 2016, 2021, and 2022 to infer temporal changes in the state of stress in the geothermal system at San Emidio. The observations support the working hypothesis that increasing pore-fluid pressure reduces the effective normal stress acting across fault zones. During normal operations, pumping in deep production wells decreases the pore-fluid pressure and increases the effective normal stresses on faults, thus modulating microseismicity. During planned shutdowns, the cessation of production increases pore-fluid pressure and reduces the effective normal stress. In this paper, we summarize the conclusions of the WHOLESCALE project.

INTRODUCTION

The WHOLESCALE team includes personnel from two universities (UW &UNR, two national laboratories (LLNL and NREL), and one industry partner (Ormat) as listed in Table 1. We count as members of the WHOLESCALE team those individuals who have performed at least two of the roles established by the Contributor Roles Taxonomy (CRediT) https://credit.niso.org/.

Background

The goal of the WHOLESCALE project is to simulate the spatial distribution and temporal evolution of stress in a geothermal system. To reach this goal, the WHOLESCALE team has developed a methodology that incorporates and interprets data from four methods of measurement into a multi-physics model that couples thermal, hydrological, and mechanical (T-H-M) processes over spatial scales ranging from the diameter of a borehole (~0.1 m) to the extent of the entire field (~10 km) and temporal scales ranging from the duration of a microseismic event (~1 second) to the typical lifetime of a producing field (3 decades).

To do so, the WHOLESCALE team has taken advantage of the perturbations created by pumping operations to infer temporal changes in the state of stress in the geothermal system. This rheological experiment applied the key idea that increasing pore-fluid pressure reduces the effective normal stress acting across preexisting faults. The work included: (1) manipulating the stress field via hydraulic and thermal methods, (2) measuring the resulting response by geophysical methods, and (3) calculating the stress, strain, pressure, and temperature in the geothermal system using an open-source, numerical simulator named GEOS.

The WHOLESCALE team has applied this methodology at the San Emidio geothermal field, located ~100 km north of Reno, Nevada in the northwestern Basin and Range province. The geology, geophysics, and geothermics have been described previously (Matlick, 1995; Rhodes et al., 2010; Warren, 2010; Eneva et al., 2011; Moeck, 2011; Rhodes, 2011; Rhodes et al., 2011; Faulds, 2014; UNR, 2014; Teplow and Warren, 2015; Pulliam et al., 2019; Reinisch et al., 2019; Warren et al., 2019; Feigl et al., 2020; Folsom et al., 2020; Folsom et al., 2021; Feigl et al., 2022; Guo et al., 2022; Jahnke, 2022; Jahnke et al., 2022; Akerley et al., 2023; Jahnke et al., 2023; Sone et al., 2023).

The San Emidio geothermal system occupies a right step in a North-striking, West-dipping, normal fault zone, as mapped in Figure 1 and Figure 2. Minor dilation and high fault density within the right step likely produce the permeability necessary for deep fluid circulation (e.g., Eneva et al., 2011). Power was first produced in 1987 with a 3.6-MW binary plant, and average production increased to 9 MW (net) following commissioning of a new power plant in 2012. Production has ranged from less than 190 L/s to more than 280 L/s at temperatures of 140–148˚C. Drilling, geological, geophysical, and geochemical data sets collected since the 1970s help constrain controls on the geothermal resource and the structural setting.

At San Emidio, Ormat has provided access to four types of observational data collected by innovative techniques in seismology, drilling, geodesy, and hydrology. To interpret these rich data sets, GEOS uses the finite-element method to solve the coupled differential equations governing the physics of a fractured, poroelastic medium under stress. The study site at San Emidio includes a volume with length of ~6 km, width ~5 km, and depth ~2 km. At each point within a mesh of this volume, the resulting numerical solution determines the complete

stress tensor as a function of time as well as its sensitivity to perturbations in the input parameters. The numerical GEOS solution also calculates modeled values for each of the four types of observable quantities. By optimizing the goodness of fit between the observations and the modeled value calculated by the GEOS simulator, the methodology determines the model configuration that best fits the data and thus the best prediction of the spatial distribution and temporal evolution of the complete stress tensor.

The WHOLESCALE project should make an important impact because geothermal operators need quantitative information about the subsurface stress to successfully develop and sustainably manage a geothermal reservoir. The applied methodology has advanced capabilities "to directly measure or infer the stress state" which had been "woefully inadequate, especially away from boreholes" as noted in the funding opportunity announcement (EERE, 2019). By reducing the uncertainty of in-situ stress estimates, the WHOLESCALE project should reduce the cost of geothermal energy.

Analysis of seismic data collected in 2016

In a peer-reviewed paper, Guo et al. (2023)found enhanced microseismicity during a planned, temporary cessation of pumping operations at San Emidio in December 2016. "To quantify this association, we analyze data from a dense seismic array deployed at the San Emidio geothermal field, Nevada for 1 week in December 2016 to coincide with a 19.45-hr shutdown of all injection and production pumping operations. 123 MSEs were detected, of which 101 occurred during the shutdown. The spatial association of the MSEs with the production wells suggests a causal relationship between the production cessation and the MSEs. Here we performed a detailed analysis to investigate reservoir material properties, distribution of seismically activated faults, and local stress state. We determined the hypocenters, magnitudes, and focal mechanisms for the MSEs, P-wave tomographic velocity model, and local stress tensor. The results show that most MSEs occurred near the production wells. Magnitudes fall between –2.2 and 0.0 with larger events located closer to the production wells. Most MSEs occurred within a westward-dipping normal fault zone in the reservoir associated with anomalously low P-wave velocity values. The focal mechanism and stress inversion results show predominantly normal faulting with the maximum horizontal stress oriented north-south. We suggest that the MSEs during shutdown were triggered on pre-existing, small-scale, critically stressed fault patches in the reservoir as the pore pressure increased around the production wells when the production pumping ceased. We interpret the larger MSE magnitudes closer to the production wells as a result of higher pore pressure increase." (Guo et al., 2023).

Analysis of seismic data collected in 2022

In a second peer-reviewed paper, (2025) analyzed data from a dense seismic and hydrologic monitoring system deployed at San Emidio to accompany a planned power plant shutdown in April 2022. "Using the dense seismic array data, we detected and located ~1,800 microseismic events (MSEs) and developed a high-resolution tomographic P-wave velocity model. We observed substantially increased microseismicity during shutdown. Most MSEs occurred on pre-existing normal faults, which are contained within extremely low-velocity zones that are likely damaged, fluid-filled, and hydraulically connected to nearby production wells. Hydrologic data show rapid fluid pressure increases of <60 kPa following the shutdown. We suggest that the cessation of production rapidly increased fluid pressures along pre-existing fault zones, activating critically stressed fault patches and fractures and producing microseismicity."(Guo et al., 2025).

"We detected and successfully located 1,761 microseismic events (MSEs), 134 of which occurred before shutdown, 1,575 during shutdown, and 52 after restart. All these events have small magnitudes between -3 to 1. Because our detection was likely affected by temporarily varying noise levels, which were considerably lower when the pumps were off, we defined a magnitude threshold of –0.6, above which the detection capability is comparable during periods of normal operations and shutdown based on the magnitude-frequency distribution. Above magnitude–0.6, there are 69 events (0.2 events per hour) before shutdown, 278 events (3.4 per hour) during shutdown, and 12 events (0.04 per hour) after restart, indicating a significant increase in microseismicity during shutdown. The two largest events with magnitudes of 1.08 and 1.11 occurred 52 hours after shutdown. The maximum event magnitude during normal operations is 0.98, ~230 hours before shutdown." (Guo et al., 2025).

Calibration of long-term T-H-M model on geodetic observations

To describe the geodetic data analyzed in previous tasks, we have developed a fully coupled, thermo-hydro-mechanical (T-H-M) numerical model using the open-source GEOS code developed at Lawrence Livermore National Laboratory (e.g., Liu et al., 2018; Settgast et al., 2018). To incorporate the 3-dimenstional structure, we have built a tessellated mesh composed of tetrahedral, finite elements (Luo et al., 2024). For the mechanical and hydrologic aspects of the model, we use the same material properties, initial conditions, and boundary conditions as assumed for the short-term H-M model (Luo et al., 2024). The modeled viscosity of water is assumed to be constant, i.e. it does not vary with temperature. For the thermal aspects of the modeling, we assume material properties and boundary conditions that are consistent with previous studies. The initial conditions are set to the "natural state" temperatures before production began (Folsom et al., 2022). The modeling results in terms of vertical displacement rate are shown in map view (Figure 5).

We have calibrated the long-term T-H-M model using geodetic observations from InSAR and GPS. We consider vertical displacement and its temporal derivative, velocity. In the latter case, the observed value is the mean vertical velocity (in mm/year) from 2016 to 2022 as measured by InSAR. The modeled values are calculated from the long-term T-H-M model implemented in GEOS. The difference of these two values is the residual. The observed, modeled, and residual fields appear in map view in panels a, b, and c of Figure 5, respectively. The absolute values of the residuals are plotted as a histogram in the lower-right panel of Figure 5. The misfit statistic, i.e. the mean absolute value of the residual difference, is 1.1 mm/year for the pixels where the observed velocity is at least twice its estimated standard deviation in absolute value.

In Area C, on the playa to the west of the production wells, the modeled deformation field (Figure 5b) differs markedly from the deformation field observed by InSAR (Figure 5a). The observed deformation field shows a velocity gradient greater than 1 mm/year per kilometer where the modeled displacement field is essentially uniformly less than 2 mm/year.

In Area A, near the production wells, the shape of the modeled subsidence "bowl" (Figure 5b) roughly mimics that observed by InSAR in Sentinel-1 Track 42 (Figure 5a). The modeled rate of vertical displacement, however, is significantly higher than the observed rate. To quantify this difference, we consider the (relative) vertical displacement of a point located in the center of the geothermal field (near GPS station SEMN) with respect to a point located at the southern edge of the geothermal field (near GPS station SEMS). This rate is -28.2 ± 0.1 mm/year in the model. The InSAR estimate is –7.5 ± 0.2 mm/year, as estimated from InSAR data acquired between 2016-01-07 and 2022-06-04 in Sentinel-1 Track 42 without accounting for atmospheric effects. The InSAR estimate agrees well with the value of –7.6 ± 0.4 mm/year estimated from the GPS data between January 2021 and April 2022 by a least-squares fit. A realistic estimate of the uncertainty on both geodetic rates is more likely to be of the order of 2 mm/year.

The shape of the modeled displacement field agrees approximately with that observed by InSAR near the producing wells at the center of the geothermal field. In terms of the rate of vertical displacement, however, the T-H-M simulations are greater than the GPS and InSAR observations by a factor of ~4. Further tuning of the model parameters, especially spatial permeability, will be required to match the geodetic observations.

Calibration of the H-M model on hydrologic observations

We have calibrated the short-term H-M model using pressure measurement from a flow test conducted in 2017. The observed data set consists of pressure measurements recorded in six wells over eight days in 2017 as shown as blue dots in Figure 4. The modeled values are calculated from the short-term H-M simulation computed using GEOS, as shown as black curves in Figure 4. For this calibration, the metric is the root-mean-square (RMS) scatter of the residuals accumulated over all six wells.

In this type of modeling, permeability is an extremely important parameter. We have considered many different combinations of permeability for the various regions in the short-term H-M simulation, as shown in Table 2. The RMS statistics for the different sets of input permeabilities are shown as a bar graph in Figure 3. For our preferred solution (case 40), the RMS scatter of the residual pressure values is 40.9 kPa.

Calibration of short-term H-M model on seismic observations

We have calibrated the short-term H-M model using the timings and locations for microseismic events recorded before, during and after the shutdowns in December 2016 and April 2022. To do so, we evaluate the Coulomb failure criterion on sets of planes using the simulated stress field calculated by a GEOS solution. We assume that the rock is critically stressed during normal operations.

Following equation (3) of Oppenheimer et al. (1988), we write the proximity of a rock volume to failure as a Coulomb failure function $F = |\tau_p| - \mu(\sigma_p - p) - S_0$,where $|\tau_P|$ is the magnitude of the shear traction vector, σ_P is the normal traction (a scalar) and p is the fluid pressure inside the pores within the rock. We assume that the internal friction coefficient $\mu = 0.6$ and that cohesion $S_0 = 0$. We follow more recent conventions and denote the value of F as *CFS* and temporal *changes* in F as ΔCFS. Since the magnitude of the shear stress is always positive, *CFS* does not distinguish between dextral and sinistral shear. Similar notational conventions appear elsewhere (e.g., Vavryčuk, 2014; Kusumawati et al., 2021). Oppenheimer et al. (1988) also note that "a physical assumption implicit in the criterion is that the quantity $\sigma_p - p$ [effective stress] be greater than zero; otherwise different modes of failure will occur", citing Jaeger and Cook (1979, p. 96). To follow this sign convention, as used in rock mechanics, we multiply by –1 each component of the (effective) stress tensor output by the GEOS code.

For each location (X, Y, Z) in the model grid, the ΔCFS values are calculated with respect to an (arbitrary) reference value $CFS(t_{ref}, X, Y, Z)$ at time t_{ref}. In other words, at time t_i, the change in Coulomb failure stress $\Delta CFS(t_i, X, Y, Z) = CFS(t_i, X, Y, Z) - CFS(t_{ref}, X, Y, Z)$. Since we assume critically stressed conditions at the reference time t_{ref}, a value of ΔCFS greater than an assumed critical value ΔCFS_{crit} implies that failure is favored.

Next, we calculate the modeled change ΔCFS in Coulomb failure stress on the (hypothetical) optimally oriented plane at each grid point in a 3-dimensional grid with a spacing of 100 m. The model calculates ΔCFS at each 1-hour time step in the model.

To evaluate the timings of the microseismic events, we extract the modeled change ΔCFS at the grid point nearest the precise location (X, Y) of each microseismic event at the corresponding time step in the model. For clarity, the model is evaluated at a constant elevatin H = 500 m above mean sea level, i.e. about 700 m below ground surface. Figure 6 and Figure 7 show results as time series for the shutdowns in 2016 and 2022, respectively. Of the ~1000 events during each shutdown, a majority occur when the modeled value of ΔCFS exceeds the critical value ΔCFS_{crit}.

To evaluate the locations of the microseismic events, Figure 8 and Figure 9 show the results in map view for the shutdowns in 2016 and 2022, respectively. In each case, most of the events occur in areas where the modeled value of ΔCFS exceeds the critical value ΔCFS_{crit}.

CONCLUSIONS

The rich, 4-D data sets at San Emidio constrain multiphysics T-H-M modeling. Synoptic measurements of pressure, seismicity, and deformation during three scheduled shutdowns provide information on the spatial distribution and temporal evolution of stress. The WHOLESCALE project has generated 18 publicly available data sets, as listed in Table 3.

Laboratory testing shows little or no anisotropy in seismic velocity at the centimeter scale in rock samples.

We have used the GEOS multiphysics code in two sets of simulations. The *long-term* simulations account for thermal, hydrological, and mechanical (T-H-M) processes over time scales of days to decades. The *short-term* simulations account for hydro-mechanical (H-M) processes over time scales on the order of hours to days. In both cases, the result is a modeled stress field $\sigma(t, x, y, z)$ as a function of time and position.

We find that the orientations of faults, fractures, and conductive fluid pathways produce pressure propagation that varies considerably, even between wells that are within few hundred meters of each other. In some cases, a single large aperture feature dominates the fluid flow, whereas a more distributed zone consisting of a network of fractures accommodates the fluid flow in other cases. Also, the orientations of the conductive fractures do not necessarily coincide with the overall orientation of the largest fault structures. The mechanical responses of these conductive features also vary on spatial scales of the order of hundreds of meters.

The azimuth of maximum compressive horizontal stress S_{Hmax} calculated from the long-term T-H-M simulation agrees to within 20 degrees of the orientation of drilling-induced tensile fractures (DITF) picked from a borehole image log of Well 17A-21.

Geodetic observations from GPS and InSAR data show downward vertical displacement (subsidence) at rates of 7 ± 2 mm/year near production wells. The long-term T-H-M simulations match the shape of the deformation field near the producing wells observed by InSAR. In terms of the rate of vertical displacement, however, the T-H-M simulations are greater than the GPS and InSAR observations by a factor of ~4.

Most of the microseismic events in December 2016 and April 2022 are located within 400 m of a production well at depths between 400 m and 700 m. Most of the microseismic events are observed when production is stopped.

Using the short-term H-M model, we have calculated the stress field as a function of time. We then evaluate the Coulomb failure criterion on sets of planes using the simulated stress field calculated in the GEOS solution. Assuming that the rock is critically stressed during normal operations, we derive the change in Coulomb Failure Stress ΔCFS. According to the sign convention used in rock mechanics, positive values of ΔCFS indicate conditions favorable to fault slip. The simulated change in Coulomb Failure Stress ΔCFS is positive for 28 of the 32 events (88%) during the 2016 shutdown for which focal mechanisms were determined by Guo et al. (2023).

Extending the same approach, we also calculate the modeled change ΔCFS in Coulomb failure stress on (hypothetical) optimally oriented planes at every location in the study area and at all times during the interval when seismic observations are available. The timings and locations of points when and where the simulated change in Coulomb Failure Stress ΔCFS takes a positive value are comparable to those of the microseismic events observed during the shutdown in December 2016. To perform a post-audit of the model results, we have used data from a seismic array consisting of 450 three-component seismographs deployed before, during, and after a planned shutdown in April 2022.

The observations support the working hypothesis that increasing pore-fluid pressure reduces the effective normal stress acting across fault zones. During normal operations, pumping in deep production wells decreases fluid pressures and thus increases the effective normal stresses on faults, modulating microseismicity. During planned shutdowns, the cessation of production increases pore-fluid pressure along conductive pathways that are connected to production wells, and reduces effective normal stress. As a result, microseismic events tend to occur on small-scale, critically stressed fault patches and fractures within the reservoir.

Thermoelastic effects over years are comparable to changes in hydraulic and mechanical stresses over time scales of hours to days. Changes in tectonic stress are not significant over the reservoir lifetimes. The stress analysis suggests that no major hazard is to be expected from normal operations or planned plant shutdowns.

Spatial variations in the local stress state are also observed, indicating stress heterogeneity in the reservoir. These results combine to indicate that the geothermal reservoir at San Emidio is a fractured, fluid filled, and permeable body that has developed along the existing normal faults.

Table 1. List of individuals who have contributed to the WHOLESCALE project.

Name	Title	Conceptualization	Data curation	Formal Analysis	Funding acquisition	Investigation	Methodology	Project administration	Resources	Software	Supervision	Validation	Visualization	Writing – original draft	Writing – review &	ORCID	Org.	State
Kurt Feigl	PI	1	1	1	1	1	1	1	1	1	1	1	1	1	1	https://orcid.org/0000-0002-2059-6708	UW	WI
Hiroki Sone	Co-PI	1			1	1					1			1	1	https://orcid.org/0000-0001-5525-1294	UW	WI
Jesse Hampton	Co-PI	1			1	1					1			1	1	https://orcid.org/0000-0001-8568-3100	UW	WI
Michael Cardiff	Co-PI	1			1	1					1			1	1	https://orcid.org/0000-0002-6720-6084	UW	WI
Cliff Thurber	Faculty	1		1	1	1					1			1	1	https://orcid.org/0000-0002-4940-4618	UW	WI
Herb Wang	Faculty	1			1	1					1			1	1	https://orcid.org/0000-0002-1631-4608	UW	WI
Corné Kreemer	Faculty		1		1	1					1			1	1	https://orcid.org/0000-0001-6882-9809	UNR	NV
Chris Sherman	Staff Scientist	1			1	1					1			1	1	https://orcid.org/0000-0003-3550-0657	LLNL	CA
Ian Warren	Staff Scientist (a)				1	1					1			1	1	https://orcid.org/0000-0002-5870-8891	NREL	CO
Sabrina Bradshaw	Asst Project Manager		1			1		1						1	1	https://orcid.org/0000-0002-3846-4893	UW	WI
Sui "Jay" Tung	Associate Scientist (b)			1		1				1		1		1	1	https://orcid.org/0000-0002-4708-2133	UW	WI
Hao Guo	Postdoctoral, Scientist		1	1			1			1				1	1	https://orcid.org/0000-0001-8287-3689	UW	WI
Ben Heath	Postdoctoral (c)			1			1			1						https://orcid.org/0000-0002-9460-3042	UW	WI
Erin Cunningham	Postdoctoral (d)			1			1			1						https://orcid.org/0000-0002-9680-6812	UW	WI
Xi Luo	Postdoctoral (e)			1			1			1						https://orcid.org/0009-0004-6401-9971	UW	WI
Matteo Cusini	Postdoctoral									1						https://orcid.org/0000-0002-6024-861X	LLNL	CA
Oddy Mudatsir	Graduate Student			1									1			https://orcid.org/0009-0005-8958-3381	UW	WI
Zirou Jin	Graduate Student					1										https://orcid.org/0000-0001-7056-8281	UW	WI
Collin Roland	Graduate Student (f)		1				1			1						https://orcid.org/0000-0003-1004-0746	UW	WI
Ben Jahnke	Graduate Student (g)		1											1	1	https://orcid.org/0000-0002-1837-7522	UW	WI
Samantha Kleich	Graduate Student (h)			1		1								1	1	https://orcid.org/0000-0002-5999-0710	UW	WI
Anya Wolterman	Research Specialist (i)		1			1				1						https://orcid.org/0000-0003-4250-578X	UW	WI
Sam Batzli	Staff Scientist		1													https://orcid.org/0000-0002-9597-5614	UW	WI
Neal Lord	Technician		1			1										https://orcid.org/0000-0003-1457-0381	UW	WI
Peter Sobol	Technician		1			1										https://orcid.org/0009-0003-2083-6323	UW	WI
John Murphy	Resource Manager					1			1							https://orcid.org/0000-0003-4911-0027	Ormat	NV
John Akerley	Resource Manager	1			1				1							https://orcid.org/0000-0001-7055-3450	Ormat	NV
Matthew Folsom	Project Geophysicist (j)			1										1	1	https://orcid.org/0000-0002-9079-6684	Ormat	NV
Courtney Brailo	Project Geologist				1	1										https://orcid.org/0009-0000-6156-7762	Ormat	NV
Gabrielle Ramirez	Project Geologist				1	1										http://orcid.org/0009-0007-7271-9208	Ormat	NV

(a) now Principal Geoscientist at Zanskar Geothermal & Minerals, ID
(b) now Assistant Professor at Texas Tech University, TX
(c) now Duty Scientist at National Tsunami Warning Center, AK
(d) now Geophysicist at now at Oak Ridge National Laboratory, TN
(e) now pursuing Master's Degree in Data Science
(f) now Hydrologist at U.S. Geologic Survey
(g) now Associate Geologist at Cella Mineral Storage, NY
(h) now Geotech Staff now at Shannon & Wilson, OR
(i) now pursuing Master's Degree Civil & Environmental Engineering
(j) now Senior Project Geoscientist at Geologica

University of Wisconsin-Madison (UW) http://geoscience.wisc.edu/
University of Nevada-Reno (UNR) http://geodesy.unr.edu/
Lawrence Livermore National Laboratory (LLNL) https://www.llnl.gov/
National Renewable Energy Laboratory (NREL) https://www.nrel.gov/
Ormat Technologies, Inc. (Ormat) http://www.ormat.com/

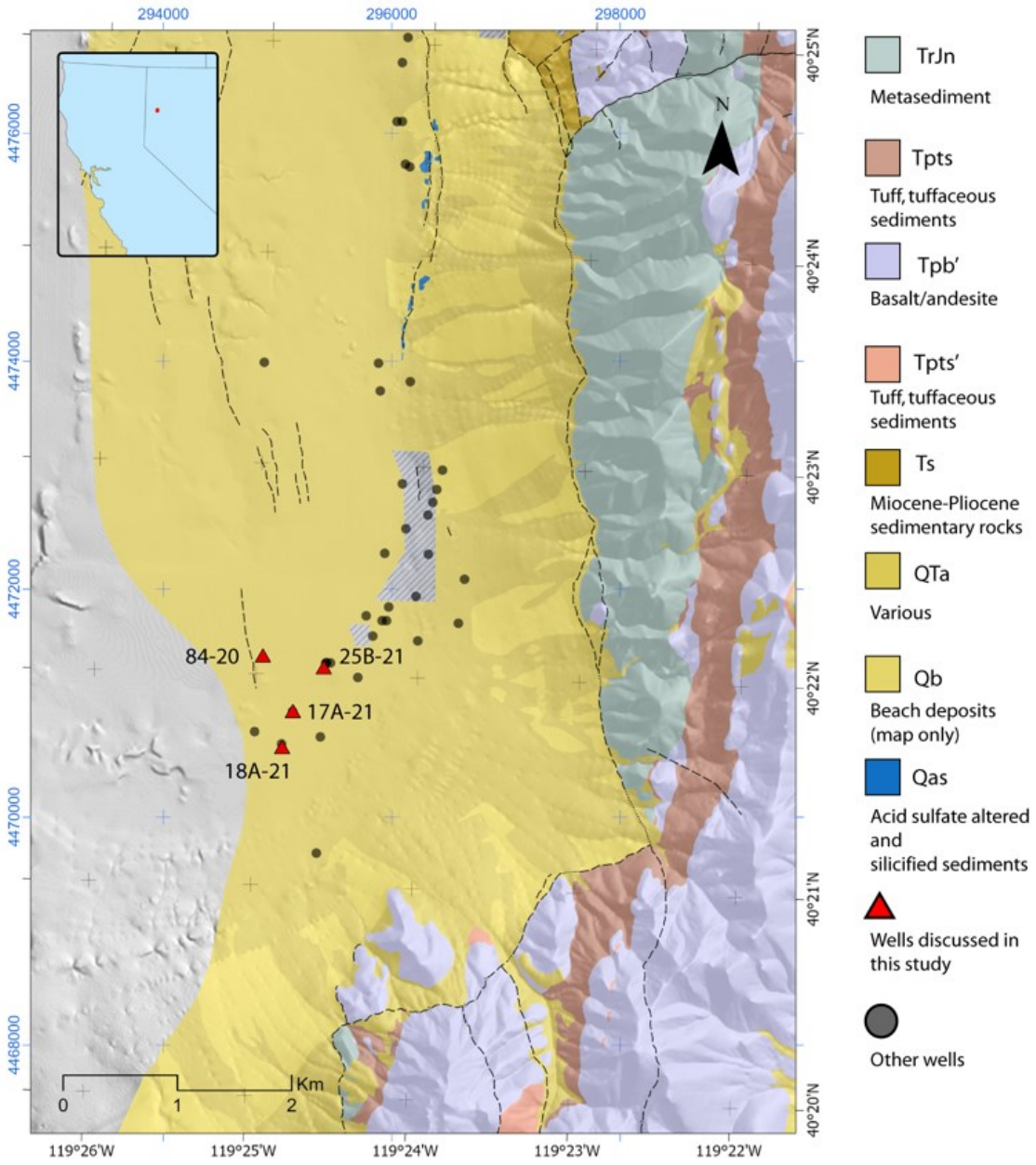

Figure 1. Geologic map of field area. As part of the North Valley Project in the San Emidio geothermal area, Ormat has drilled three new production wells (17A-21, 18A-21, and 25B-21) and a new injection well (84-20), shown as red triangles. Other wells are shown as circles. Geologic units simplified from earlier work (Rhodes, 2011; Rhodes et al., 2011) by Matt Folsom (2020). Black tick marks and labels on the east and south edges give geographic (WGS84) latitude and longitude, respectively in degrees and minutes. Blue ticks and labels on north and west edges give easting and northing coordinates, respectively, in meters in Zone 11 of the Universal Transverse Mercator (UTM) projection.

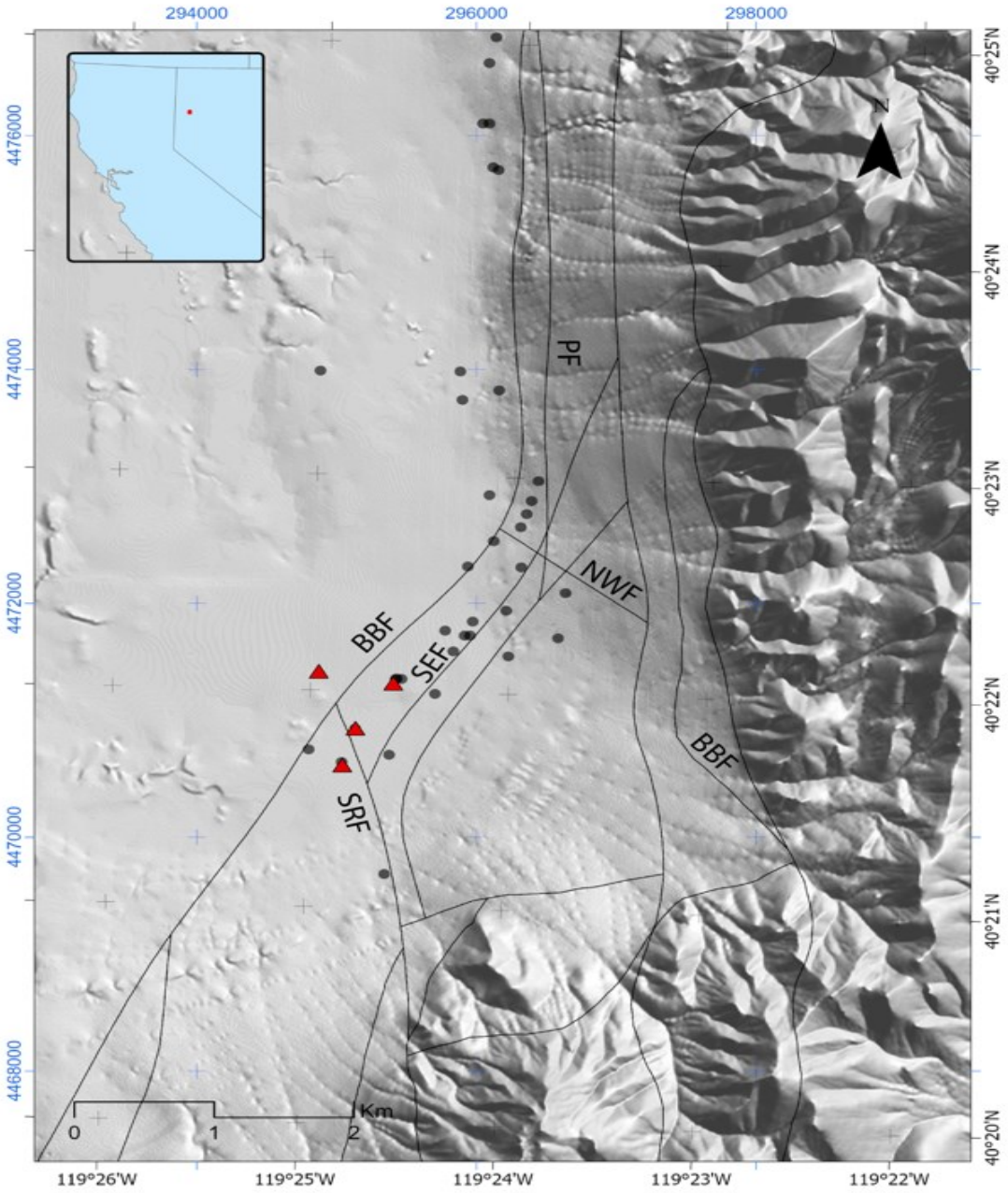

Figure 2. Map of the WHOLESCALE study area at San Emidio, showing fault traces in the geologic structural model updated in 2022 by Matt Folsom. The background gray image shows the topography. New production wells (17A-21, 18A-21, and 25B-21) and a new injection well (84-20) are shown as red triangles. Other wells are shown as circles. Fault names include: RFF, Range front fault; NF, Nightingale fault; FF, Fan fault; AF, Antithetic fault; SEF, San Emidio fault; BBF, Basin Bounding fault; PF, Piedmont fault; NWF, NW fault. Black tick marks and labels on the east and south edges give geographic (WGS84) latitude and longitude, respectively in degrees and minutes. Blue ticks and labels on north and west edges give easting and northing coordinates, respectively, in meters in Zone 11 of the Universal Transverse Mercator (UTM) projection.

Table 2. Summary of permeability of rock formations for GEOS model input cases.

case number	TRMS [kPa]	QTA	QTA	QTA	QAS	QAS	QAS	TPTS	TPTS	TPTS	TPTSPR	TPTSPR	TPTSPR	TRJN	TRJN	TRJN	TS	TS	TS	fault_ee	fault_ee	fault_ee	fault_ee	fault_ee	fault_ee	fault_bd	fault_bd	fault_bd
permeability	[m^2]	kx	ky	kz	kx	ky	kz	kx	ky	kz	kx	ky	kz	kx	ky	kz	kx	ky	kz	kx	ky	kz	kx	ky	kz	kx	ky	kz
1	91.8	1.5E-12	1.5E-12	1.1E-14	4.3E-11	4.3E-11	3.1E-13	1.7E-12	1.7E-12	1.7E-12	2.4E-11	2.4E-11	2.4E-11	3.1E-14	3.1E-14	3.1E-14	3.1E-14	3.1E-14	3.1E-14									
2	91.8	1.5E-12	1.5E-12	7.5E-13	4.3E-11	4.3E-11	2.2E-11	1.7E-12	1.7E-12	1.7E-12	2.4E-11	2.4E-11	2.4E-11	3.1E-14	3.1E-14	3.1E-14	3.1E-14	3.1E-14	3.1E-14									
3	89.3	1.5E-12	1.5E-12	5.0E-13	4.3E-11	4.3E-11	1.4E-11	1.7E-12	1.7E-12	1.7E-12	2.4E-11	2.4E-11	2.4E-11	3.1E-14	3.1E-14	3.1E-14	3.1E-14	3.1E-14	3.1E-14									
4	39.8	1.5E-13	1.5E-13	4.3E-14	8.2E-11	8.2E-11	1.8E-11	1.3E-13	1.3E-13	3.7E-14	5.2E-11	5.2E-11	1.5E-11	4.4E-14	4.4E-14	1.3E-14	4.4E-14	4.4E-14	1.3E-14									
5	56.4	1.5E-13	1.5E-13	4.3E-14	8.2E-11	8.2E-11	1.8E-11	1.3E-13	1.3E-13	3.7E-14	2.4E-12	2.4E-12	8.9E-13	4.4E-14	4.4E-14	1.3E-14	4.4E-14	4.4E-14	1.3E-14									
6	59.5	1.5E-13	1.5E-13	4.3E-14	8.2E-11	8.2E-11	1.8E-11	1.3E-13	1.3E-13	3.7E-14	5.2E-11	5.2E-11	1.5E-11	4.4E-15	4.4E-15	1.3E-15	4.4E-14	4.4E-14	1.3E-14									
7	54.9	1.5E-13	1.5E-13	4.3E-14	8.2E-11	8.2E-11	1.8E-11	1.3E-13	1.3E-13	3.7E-14	5.2E-11	5.2E-11	1.5E-11	4.4E-15	4.4E-15	1.3E-15	4.4E-15	4.4E-15	1.3E-15									
8	41.9	1.5E-13	1.5E-13	4.3E-14	8.2E-11	8.2E-11	1.8E-11	1.3E-14	1.3E-14	3.7E-15	5.2E-11	5.2E-11	1.5E-11	4.4E-14	4.4E-14	1.3E-14	4.4E-14	4.4E-14	1.3E-14									
9	53.4	1.5E-13	1.5E-13	4.3E-14	8.2E-11	8.2E-11	1.8E-11	1.7E-12	1.7E-12	1.7E-12	1.3E-13	1.3E-13	3.7E-14	4.4E-14	4.4E-14	1.3E-14	4.4E-14	4.4E-14	1.3E-14									
10	48.4	1.5E-13	1.5E-13	4.3E-14	8.2E-11	8.2E-11	1.8E-11	1.7E-12	1.7E-12	1.7E-12	1.3E-13	1.3E-13	3.7E-14	4.4E-14	4.4E-14	1.3E-14	4.4E-14	4.4E-14	1.3E-14	1.5E-10	1.5E-10	1.5E-10	1.5E-10	1.5E-10	1.5E-10			
11	48.3	1.5E-13	1.5E-13	4.3E-14	8.2E-11	8.2E-11	1.8E-11	1.3E-13	1.3E-13	3.7E-14	1.3E-13	1.3E-13	3.7E-14	4.4E-14	4.4E-14	1.3E-14	4.4E-14	4.4E-14	1.3E-14	1.5E-10	1.5E-10	1.5E-10	1.5E-10	1.5E-10	1.5E-10			
12	48.1	1.5E-13	1.5E-13	4.3E-14	8.2E-11	8.2E-11	1.8E-11	1.3E-14	1.3E-14	3.7E-15	1.3E-13	1.3E-13	3.7E-14	4.4E-14	4.4E-14	1.3E-14	4.4E-14	4.4E-14	1.3E-14	1.5E-10	1.5E-10	1.5E-10	1.5E-10	1.5E-10	1.5E-10			
13	44.8	1.5E-13	1.5E-13	4.3E-14	8.2E-11	8.2E-11	1.8E-11	1.7E-12	1.7E-12	1.7E-12	1.3E-13	1.3E-13	3.7E-14	4.4E-14	4.4E-14	1.3E-14	4.4E-14	4.4E-14	1.3E-14	1.5E-11	1.5E-11	1.5E-11	1.5E-11	1.5E-11	1.5E-11			
14	52.2	1.5E-12	1.5E-12	4.3E-13	8.2E-11	8.2E-11	1.8E-11	1.7E-12	1.7E-12	1.7E-12	1.3E-13	1.3E-13	3.7E-14	4.4E-14	4.4E-14	1.3E-14	4.4E-14	4.4E-14	1.3E-14	1.5E-11	1.5E-11	1.5E-11	1.5E-11	1.5E-11	1.5E-11			
15	120.1	1.5E-13	1.5E-13	4.3E-14	8.2E-11	8.2E-11	1.8E-11	1.3E-13	1.3E-13	3.7E-14	5.2E-11	5.2E-11	1.5E-11	4.4E-14	4.4E-14	1.3E-14	4.4E-14	4.4E-14	1.3E-14	1.5E-12	1.5E-12	1.1E-14	1.5E-12	1.5E-12	1.1E-14	1.5E-10	1.5E-10	1.5E-10
16	47.9	1.5E-13	1.5E-13	4.3E-14	8.2E-11	8.2E-11	1.8E-11	1.3E-13	1.3E-13	3.7E-14	5.2E-11	5.2E-11	1.5E-11	4.4E-14	4.4E-14	1.3E-14	4.4E-14	4.4E-14	1.3E-14	1.5E-12	1.5E-12	1.1E-14	1.5E-12	1.5E-12	1.1E-14	1.5E-11	1.5E-11	1.5E-11
17	49.2	1.5E-13	1.5E-13	4.3E-14	8.2E-11	8.2E-11	1.8E-11	1.3E-13	1.3E-13	3.7E-14	5.2E-11	5.2E-11	1.5E-11	4.4E-14	4.4E-14	1.3E-14	4.4E-14	4.4E-14	1.3E-14	1.5E-12	1.5E-12	1.5E-12	1.5E-12	1.5E-12	1.5E-12	1.5E-11	1.5E-11	1.5E-11
18	47.9	1.5E-13	1.5E-13	4.3E-14	8.2E-11	8.2E-11	1.8E-11	1.3E-13	1.3E-13	3.7E-14	5.2E-11	5.2E-11	1.5E-11	4.4E-14	4.4E-14	1.3E-14	4.4E-14	4.4E-14	1.3E-14	1.5E-12	1.5E-12	1.5E-13	1.5E-12	1.5E-12	1.5E-13	1.5E-11	1.5E-11	1.5E-11
20	38.9	1.5E-13	1.5E-13	4.3E-14	8.2E-11	8.2E-11	1.8E-11	1.3E-13	1.3E-13	3.7E-14	5.2E-11	5.2E-11	1.5E-11	4.4E-14	4.4E-14	1.3E-14	4.4E-14	4.4E-14	1.3E-14	1.5E-12	1.5E-12	1.5E-13	1.5E-12	1.5E-12	1.5E-13	1.5E-12	1.5E-12	1.5E-12
21	38.1	1.5E-13	1.5E-13	4.3E-14	8.2E-11	8.2E-11	1.8E-11	1.3E-13	1.3E-13	3.7E-14	5.2E-11	5.2E-11	1.5E-11	4.4E-14	4.4E-14	1.3E-14	4.4E-14	4.4E-14	1.3E-14	1.5E-12	1.5E-12	1.5E-13	1.5E-12	1.5E-12	1.5E-13	1.5E-13	1.5E-13	1.5E-13
22	39.8	1.5E-13	1.5E-13	4.3E-14	8.2E-11	8.2E-11	1.8E-11	1.3E-13	1.3E-13	3.7E-14	5.2E-11	5.2E-11	1.5E-11	4.4E-14	4.4E-14	1.3E-14	4.4E-14	4.4E-14	1.3E-14	1.5E-12	1.5E-12	1.0E-14	1.5E-12	1.5E-12	1.0E-14	1.5E-13	1.5E-13	1.5E-12
23	44.7	1.5E-13	1.5E-13	4.3E-14	8.2E-11	8.2E-11	1.8E-11	1.3E-13	1.3E-13	3.7E-14	5.2E-11	5.2E-11	1.5E-11	4.4E-13	4.4E-13	1.3E-13	4.4E-14	4.4E-14	1.3E-14	1.5E-12	1.5E-12	1.0E-14	1.5E-12	1.5E-12	1.0E-14	6.0E-11	6.0E-11	6.0E-11
24	48.8	1.5E-13	1.5E-13	4.3E-14	8.2E-11	8.2E-11	1.8E-11	1.3E-13	1.3E-13	3.7E-14	5.2E-11	5.2E-11	1.5E-11	4.4E-13	4.4E-13	1.3E-13	4.4E-14	4.4E-14	1.3E-14	1.5E-12	1.5E-12	1.0E-14	1.5E-12	1.5E-12	1.0E-14	6.0E-12	6.0E-12	6.0E-12
25	38.5	1.5E-13	1.5E-13	4.3E-14	8.2E-11	8.2E-11	1.8E-11	1.3E-13	1.3E-13	3.7E-14	5.2E-11	5.2E-11	1.5E-11	1.4E-14	1.4E-14	1.3E-14	4.4E-14	4.4E-14	1.3E-14	1.5E-12	1.5E-12	1.0E-14	1.5E-12	1.5E-12	1.0E-14	8.0E-12	8.0E-12	8.0E-12
40	36.8	1.5E-13	1.5E-13	4.3E-14	6.2E-11	6.2E-11	1.8E-11	1.3E-14	1.3E-14	3.7E-15	1.2E-10	1.2E-10	4.1E-11	1.4E-14	1.4E-14	3.3E-15	4.4E-14	4.4E-14	1.3E-14	1.5E-12	1.5E-12	1.5E-13	1.5E-12	1.5E-12	1.5E-13	1.5E-10	1.5E-10	1.5E-13

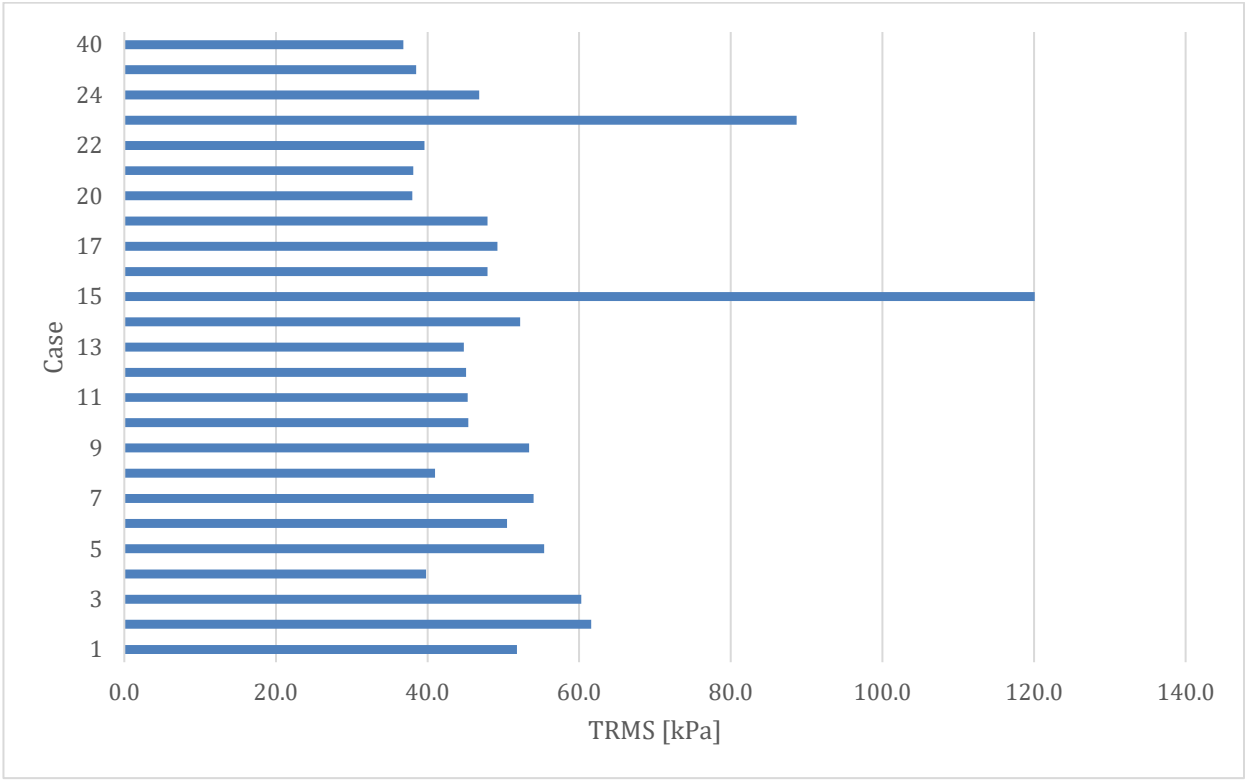

Figure 3. Overall ("total") RMS of residual pressure in kPa for each permeability.

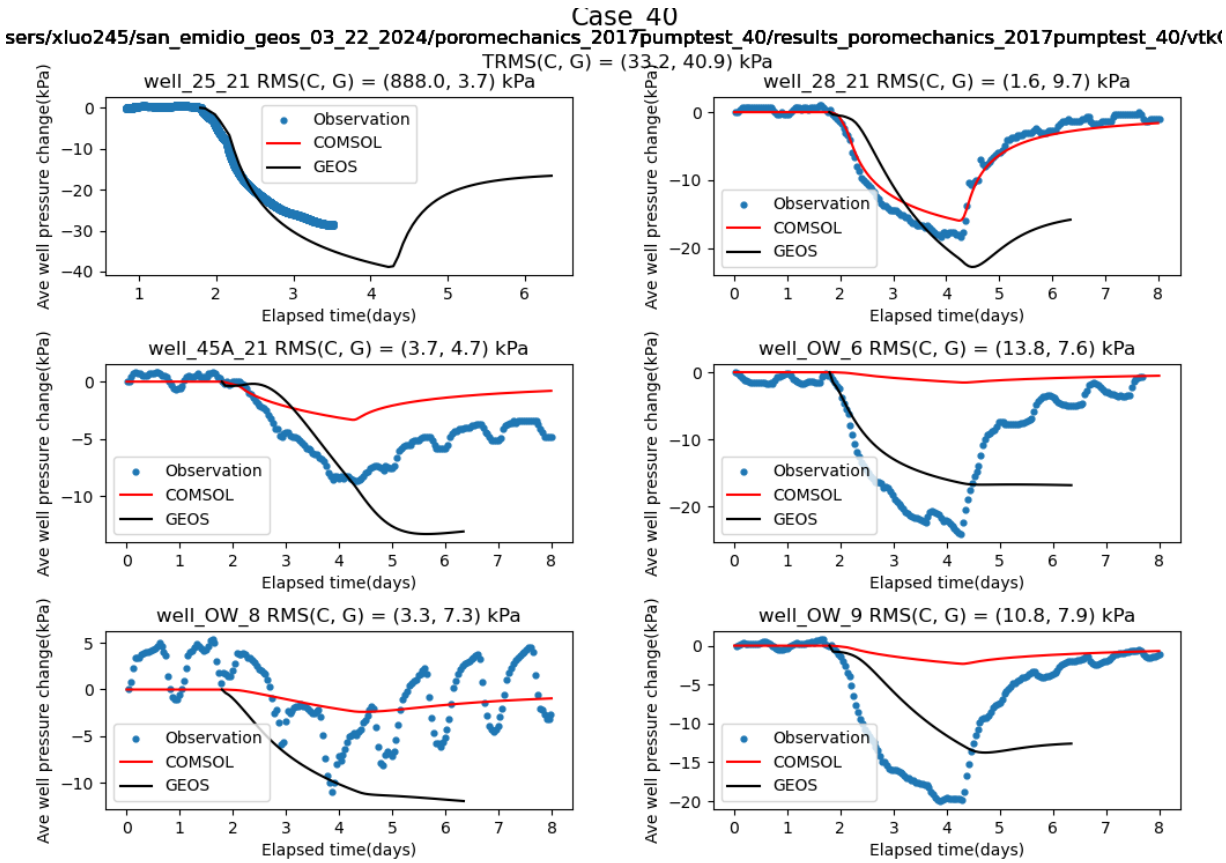

Figure 4. Pressure changes in observation wells during a flow test in 2017, showing observed pressure as blue dots, simulated pressure calculated using a hydrology-only model with COMSOL (Cardiff et al., 2023) as red curves, modeled pressure calculated using the hydro-mechanical simulation with GEOS (case 40) as black curves. The title and subtitles give the total root-mean-square (TRMS) and root-mean-square (RMS) residual difference between observed and simulated pressure values for the COMSOL (C) and GEOS (G) models respectively.

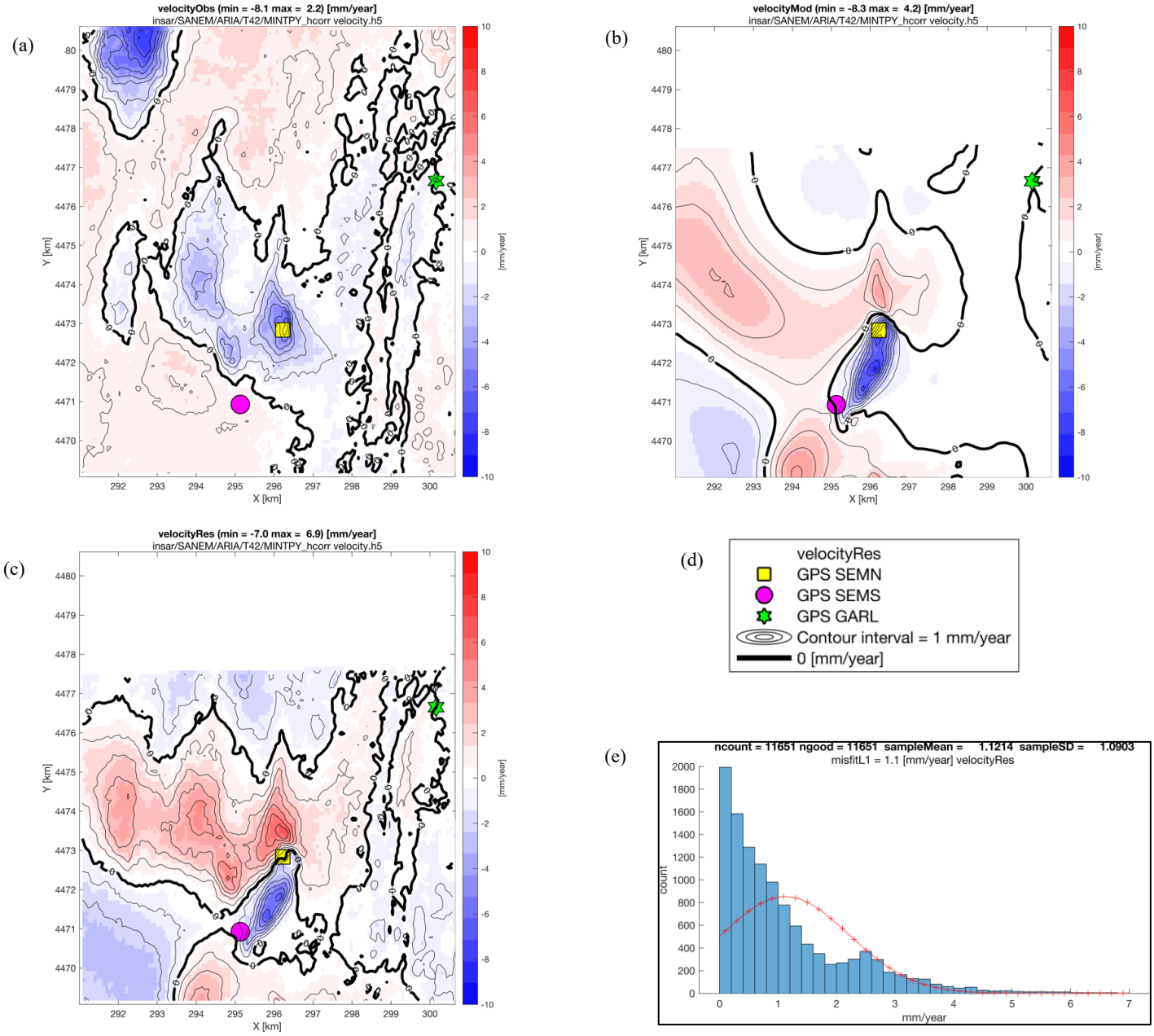

Figure 5. Map view of the mean vertical velocity (in mm/year) from 2016 to 2022 as observed by InSAR (a), as modeled by the long-term T-H-M solution in GEOS (b), and displayed as the residual difference of the modeled minus the observed fields (c). The map coordinates are Easting and Northing in the UTM cartographic projection. A legend for the three maps appears in panel (d). A histogram of the absolute values of the residual differences appears in panel (e). The red curve shows a normal distribution with mean of 1.1 mm/year and sample standard deviation of 1.1 mm/year.

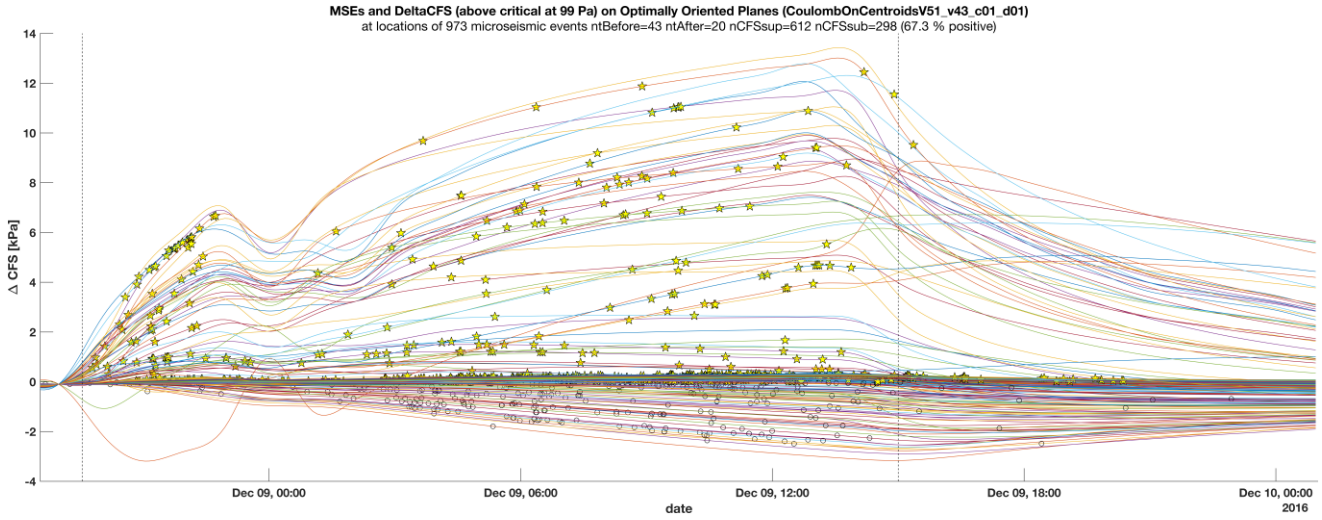

Figure 6. Time series of the change in Coulomb failure stress ΔCFS (above a critical value of ΔCFS_{crit} = 99 Pa) on hypothetical optimally orientated planes. The calculation includes the microsesmic events during the 2016 shutdown that have been precisely relocated using the REST workflow (Thurber et al. 2024; manuscript in preparation).

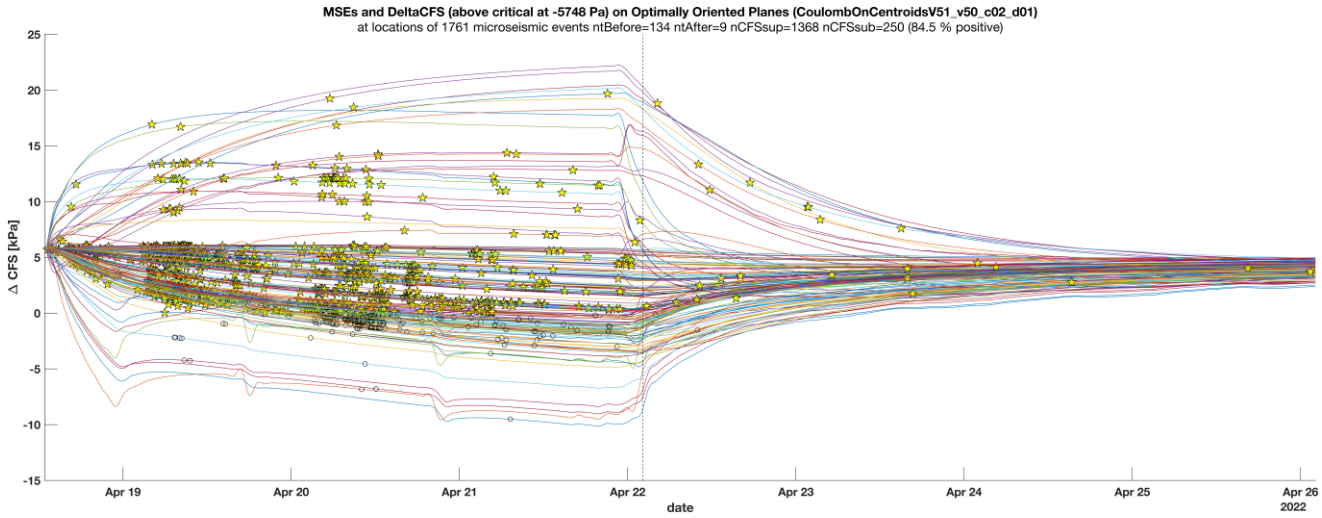

Figure 7. Time series of the change in Coulomb failure stress ΔCFS (above a critical value of ΔCFS_{crit} = –5748 Pa) on hypothetical optimally orientated planes. The calculation includes the microsesmic events during the 2022 shutdown for which precise locations are available (Guo et al., 2025).

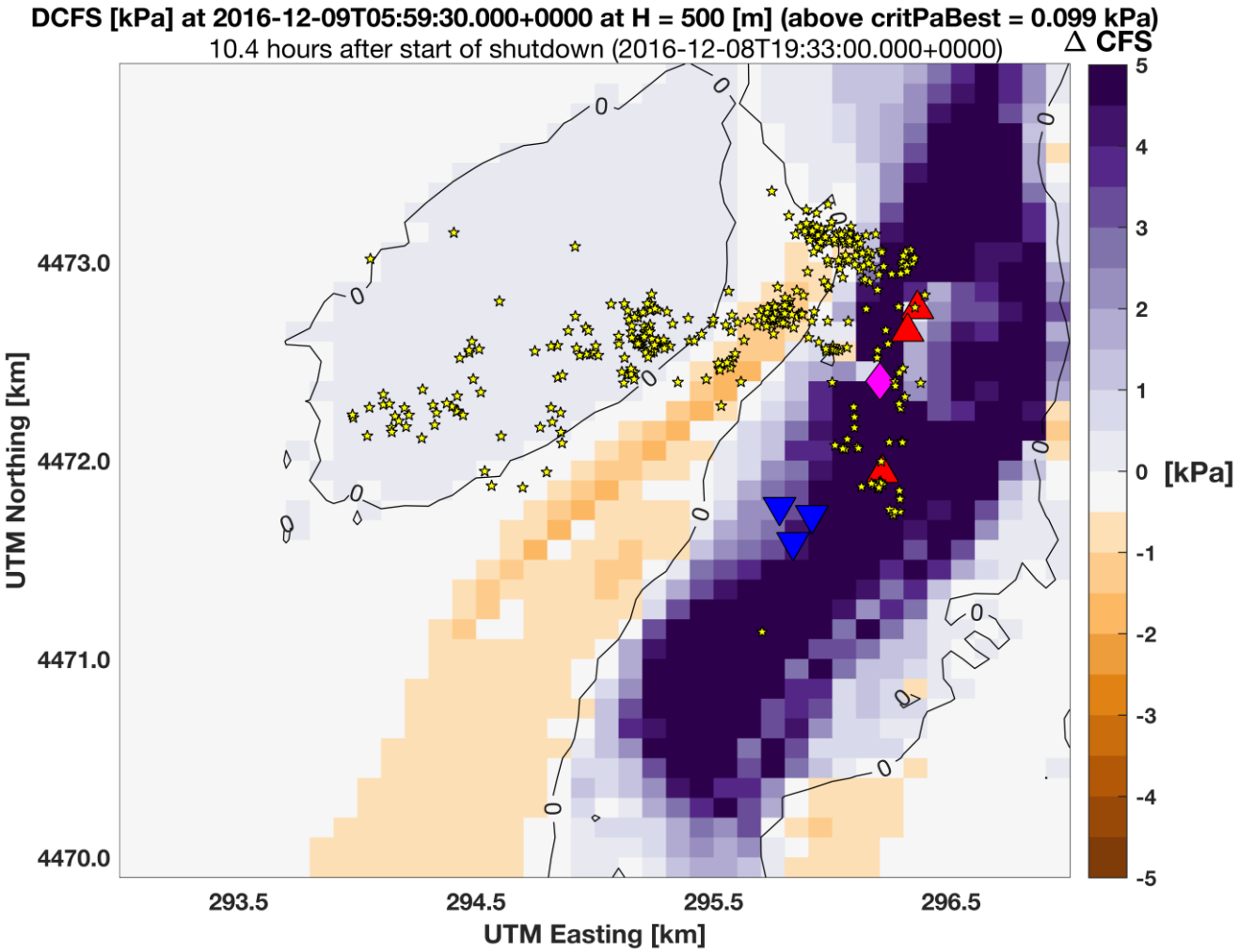

Figure 8. Numerical solution for changes ΔCFS in Coulomb failure stress in response to the shutdown of reservoir operations in December 2016. The horizontal slice at a constant elevation H = 500 m above mean sea level shows the modeled values of ΔCFS calculated at t_i = 2016/12/09 00:59:30 UTC, i.e. 5.4 hours after the shutdown began. The reference time is t_{ref} = 2016/12/08 18:33 UTC, i.e., one hour before the shutdown began. Yellow stars indicate precise locations of microseismic events that occurred during the time interval $t \in [t_{ref}, t_i]$ that have been precisely relocated using the REST workflow (Thurber et al. 2024; m.s. in preparation). The modeled values of ΔCFS (above a critical value of ΔCFS_{crit} = 99 Pa) are calculated at an elevation H = 500 m above the WGS84 geoid, i.e. depths of approximately 700 m below the ground surface. Triangles indicate wells: red for production, blue for injection. The magenta lozenge indicates the location of a representative point located near the primary production wells.

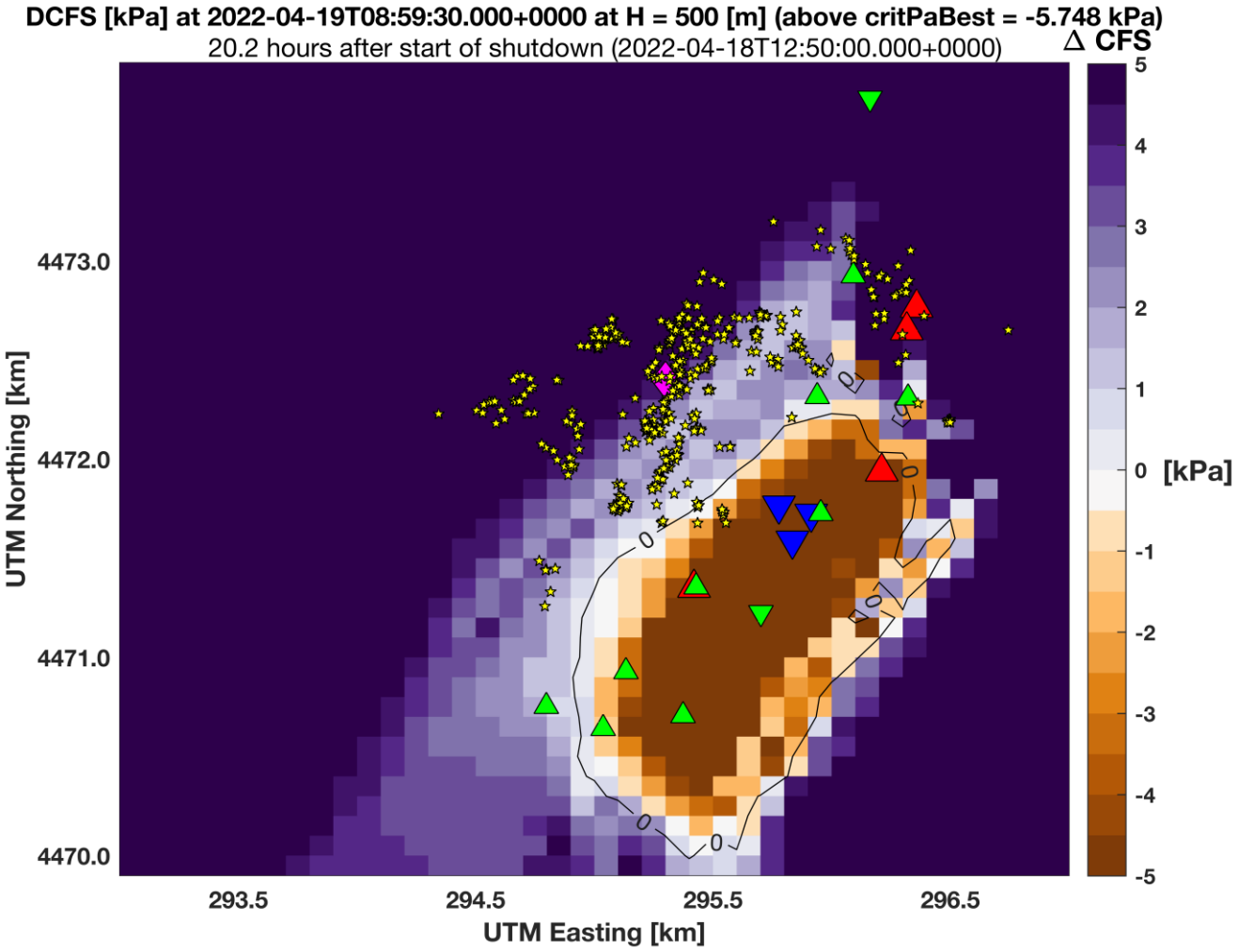

Figure 9. Numerical solution for changes ΔCFS in Coulomb failure stress in response to the shutdown of reservoir operations in April 2022. The horizontal slice shows the modeled values of ΔCFS calculated at t_i = 2022/04/19 00:59:30 UTC, i.e. 20.2 hours after the shutdown began. The reference time is t_{ref} = 2022-04-18 12:50:00, i.e., when the shutdown began. Yellow stars indicate precise locations of microseismic events that occurred during the time interval $t \in [t_{ref}, t_i]$ (Guo et al., 2025). The modeled values of ΔCFS (above a critical value of ΔCFS_{crit} = –5748 Pa) are calculated at an elevation H = 500 m above the WGS84 geoid, i.e. depths of approximately 700 m below the ground surface. Triangles indicate wells: red for production, blue for injection, green for observation. The magenta lozenge indicates the location of a representative point located at the epicenter of an microseismic event.

Table 3. Publicly available data products generated by WHOLESCALE project

Title	DOI
Passive Seismic Emission Tomography Results at San Emidio Nevada.	https://dx.doi.org/10.15121/1924268
Seismic Survey 2016 Metadata at San Emidio, Nevada	https://dx.doi.org/10.15121/1872549
Seismic Survey 2016 data at San Emidio Nevada	https://dx.doi.org/10.15121/2008357
WHOLESCALE Catalog of Rock Samples at San Emidio Nevada collected in January 2021 Version	https://dx.doi.org/10.15121/1879102
WHOLESCALE Catalog of Rock Samples at San Emidio Nevada collected in January 2021.	https://dx.doi.org/10.15121/1838419
GPS Station RINEX Files and Position Time-Series.	https://gdr.openei.org/submissions/1338
Magnetotelluric Data Collected in 2016 over the San Emidio Geothermal Field in Nevada.	https://dx.doi.org/10.15121/1974786
WHOLESCALE: Mass Flux Rates for Wells at San Emidio in December 2016	https://dx.doi.org/10.15121/2006850
WHOLESCALE: Coordinates of wells at San Emidio, Nevada	https://dx.doi.org/10.15121/2006837
WHOLESCALE: Microseismic Event Catalog for San Emidio, Nevada 2022. United States	https://dx.doi.org/10.15121/2373193
WHOLESCALE: Seismic Survey Data from San Emidio Nevada 2021	https://dx.doi.org/10.15121/2349480
WHOLESCALE: Seismic Survey Metadata from San Emidio Nevada 2021	https://dx.doi.org/10.15121/2349481
WHOLESCALE: Seismic Waveform Data from San Emidio, Nevada 2022	https://gdr.openei.org/submissions/1610
2022 seismic metadata	https://doi.org/10.7914/m5qt-mh37
P-wave velocity tomography estimated from seismic data collected in December 2016	https://doi.org/10.1029/2023JB027008
Catalog of microseismic events in December 2016, including event origin times, relocations,	https://doi.org/10.1029/2023JB027008
Microseismic Event Catalog and 3-D P-Wave Velocity Model for San Emidio, Nevada 2022	http://dx.doi.org/10.5281/zenodo.14695233

ACKNOWLEDGMENTS

The WHOLESCALE team thanks the following individuals at Ormat Technologies, Inc: Curtis Peach, Cliff Reed, Joe Pavone, Manolo Di Donato, Leeta Miller, Alan Pinuelas-Molina, David Schwab, Lupé Gonsalez Ortiz, Zack Young, and Robin Zuza. We thank the individuals who contributed to the field work: DJ Bustos (PASSCAL), Alan Horton (PASSCAL), Zirou Jin (UW-Madison), Nina Miller (UNR), and Bret Pecoraro (UNR).We thank Steven Roecker for helping us with running the REST software workflow.

The work presented herein has been funded by the Office of Energy Efficiency and Renewable Energy (EERE), U.S. Department of Energy, under Award Number DE-EE0009032.

For the 2022 seismic survey, seismic instruments were provided by the EarthScope Primary Instrument Center (EPIC, formerly the IRIS PASSCAL Instrument Center) at New Mexico Tech. Data collected during this experiment are available through the IRIS Data Management Center. "The facilities of the EarthScope Consortium are supported by the National Science Foundation under Cooperative Agreement EAR-0552316 and by the Department of Energy National Nuclear Security Administration.[1]

"Some of the results for this study were generated using Seequent software. Seequent is the Bentley Systems subsurface company."

This study includes SAR images acquired by TerraSAR-X and TanDEM-X satellite missions operated by the German Space Agency (DLR). These data were used under the terms and conditions of Research Project RES1236.

Access to data from the SENTINEL-1 satellite mission operated by the European Space Agency was provided free of charge as described by the Updated ESA Earth Observation Data Policy (Simplified version)[2].

"NASA's provision of the complete ESA Sentinel-1 synthetic aperture radar (SAR) data archive through the ASF DAAC is by agreement between the U.S. State Department and the European Commission (EC). As part of the Earth-observation Copernicus program, the Sentinel mission will provide scientists with accurate, timely, and easily accessible information to help shape the future of our planet. Content on ASF's Sentinel web pages is adapted from the ESA Sentinel-1 website"[3]

Passive seismic data collections were completed at San Emidio in late 2016 by Microseismic Inc. as part of DOE project number DE-EE0007698 as described on the metadata available in the GDR[4].

Parts of this work were performed under the auspices of the U.S. Department of Energy by Lawrence Livermore National Laboratory under Contract DE-AC52-07NA27344.

[1] https://www.passcal.nmt.edu/content/general-information/policy/instrument-use-agreement

[2] https://earth.esa.int/eogateway/documents/d/earth-online/esa-eo-data-policy

[3] https://asf.alaska.edu/datasets/daac/sentinel-1/

[4] https://gdr.openei.org/submissions/1386

DISCLAIMER

REFERENCES

Akerley, J., I. Warren, E. Gasperikova, and S. Pullammanappallil (2023), A Novel Approach to Map Permeability Using Passive Seismic Emission Tomography, United States. https://www.osti.gov/biblio/1986084

Cardiff, M., C. Sherman, H. Guo, E. Cunningham, M. Folsom, I. Warren, H. Sone, C. Thurber, H. F. Wang, and K. L. Feigl (2023), WHOLESCALE - Calibration and Simulation of hydro-mechanical Behavior at San Emidio, Nevada During Operational Changes, paper presented at Stanford Geothermal Workshop, Stanford, California. https://pangea.stanford.edu/ERE/db/GeoConf/papers/SGW/2023/Cardiff.pdf

EERE (2019), Subsurface Stress and Lost Circulation in Geothermal Drilling Funding Opportunity Announcement (FOA) Number DE-FOA-0002083. https://eere-Exchange.energy.gov

Eneva, M., G. Falorni, W. Teplow, J. Morgan, G. Rhodes, and D. Adams (2011), Surface Deformation at the San Emidio Geothermal Field, Nevada, from Satellite Radar Interferometry, GRC Transactions, 35.

Faulds, J. E. (2014), 3D Model of the San Emidio Geothermal Area [data set], Geothermal Data Repository. https://gdr.openei.org/submissions/365.

Feigl, K. L., E. C. Reinisch, S. A. Batzli, H. Sone, M. A. Cardiff, J. C. Hampton, N. E. Lord, C. H. Thurber, H. F. Wang, and C. Sherman (2020), Spatio–Temporal Analysis of Deformation at San Emidio Geothermal Field, Nevada, USA between 1992 and 2010, paper presented at Proceedings 45th Workshop on Geothermal Reservoir Engineering Stanford University, Stanford, California, February 10-12, 2020. https://pangea.stanford.edu/ERE/db/GeoConf/papers/SGW/2020/Feigl.pdf

Feigl, K. L., S. Tung, H. Guo, E. Cunningham, J. Hampton, S. J. Kleich, B. Jahnke, B. Heath, C. Roland, M. Folsom, J. Akerley, M. Cusini, C. Sherman, I. Warren, C. Kreemer, H. Sone, M. A. Cardiff, N. E. Lord, C. H. Thurber, and H. F. Wang (2022), Overview and Preliminary Results from the WHOLESCALE project at San Emidio, Nevada, U.S., paper presented at 47th Workshop on Geothermal Reservoir Engineering, Stanford, California. https://pangea.stanford.edu/ERE/pdf/IGAstandard/SGW/2022/Feigl.pdf

Folsom, M., R. Libbey, D. Feucht, W. I., and S. Garanzini (2020), Geophysical Observations and Integrated Conceptual Models of the San Emidio Geothermal Field, Nevada., paper presented at Workshop on Geothermal Reservoir Engineering, Stanford, California, USA. https://pangea.stanford.edu/ERE/db/GeoConf/papers/SGW/2020/Folsom.pdf

Folsom, M., R. Libbey, D. Feucht, I. Warren, and S. Garanzini (2021), Geophysical observations and integrated conceptual models of the San Emidio Geothermal Field, Nevada, paper presented at Nevada Petroleum & Geothermal Society, February 4th, 2021.

Guo, H., C. H. Thurber, B. A. Heath, M. Cardiff, N. Lord, I. Warren, and K. L. Feigl (2022 of Conference), Seismic analysis of reservoir conditions for inducing seismicity at the San Emidio geothermal field, Nevada, U.S.A., abstract presented at Annual Meeting Seismological Society of America, Bellevue, WA, USA, 19-23 April 2022.

Guo, H., C. Thurber, I. Warren, B. A. Heath, M. Folsom, H. Sone, N. Lord, J. Akerley, and K. L. Feigl (2023), Enhanced Microseismicity During Production Pumping Cessation at the San Emidio Geothermal Field (Nevada, USA) in December 2016, Journal of Geophysical Research: Solid Earth, 128, e2023JB027008. https://doi.org/10.1029/2023JB027008

Guo, H., C. Thurber, E. Cunningham, M. Cardiff, N. Lord, P. Sobol, H. Wang, and K. L. Feigl (2025), Microseismicity Modulation Due to Changes in Geothermal Production at San Emidio, Nevada, USA. Geophys. Res. Lett. http://dx.doi.org/10.1029/2024GL112063

Jaeger, J. C., and N. G. W. Cook (1979), Fundamentals of Rock Mechanics, 3rd edition ed., 593 pp., Chapman and Hall, London.

Jahnke, B. (2022), Geomechanical Analysis of the Geothermal Reservoir at San Emidio, Nevada and Fracture Toughness Anisotropy of EGS Collab Testbed Rocks, M.S. thesis University of Wisconsin-Madison (H. Sone, advisor).

Jahnke, B., H. Guo, B. Heath, E. Cunningham, C. Sherman, H. Sone, I. Warren, C. Kreemer, C. H. Thurber, K. F. Feigl, and WHOLESCALE_Team (2022), Spatial-Temporal Stress Heterogeneity in the Geothermal Reservoir at San Emidio, Nevada, U.S., paper presented at 45th Workshop on Geothermal Reservoir Engineering, February 7-9, 2022, Stanford University, Stanford, California,. https://pangea.stanford.edu/ERE/pdf/IGAstandard/SGW/2022/Jahnke.pdf

Jahnke, B., H. Sone, H. Guo, C. Sherman, I. Warren, C. Kreemer, C. H. Thurber, and K. L. Feigl (2023), Geomechanical analysis of the geothermal reservoir at San Emidio, Nevada, Geothermics, 110, 102683. https://doi.org/10.1016/j.geothermics.2023.102683

Krieger, G., A. Moreira, H. Fiedler, I. Hajnsek, M. Werner, M. Younis, and M. Zink (2007), TanDEM-X: A Satellite Formation for High-Resolution SAR Interferometry, IEEE Trans. Geoscience Remote Sensing, 45, 3317-3341. http://dx.doi.org/10.1109/tgrs.2007.900693

Kusumawati, D., D. P. Sahara, S. Widiyantoro, A. D. Nugraha, M. Muzli, I. Imran, N. T. Puspito, and Z. Zulfakriza (2021), Fault Instability and Its Relation to Static Coulomb Failure Stress Change in the 2016 Mw 6.5 Pidie Jaya Earthquake, Aceh, Indonesia, Frontiers in Earth Science, 8.

Liu, F., P. Fu, R. J. Mellors, M. A. Plummer, S. T. Ali, E. C. Reinisch, Q. Liu, and K. L. Feigl (2018), Inferring Geothermal Reservoir Processes at the Raft River Geothermal Field, Idaho, USA, Through Modeling InSAR-Measured Surface Deformation, Journal of Geophysical Research: Solid Earth, 123, 3645-3666. http://dx.doi.org/10.1029/2017JB015223

Luo, X., C. Sherman, K. L. Feigl, J. Murphy, J. Akerley, H. Sone, M. A. Cardiff, J. Hampton, H. Guo, N. E. Lord, P. E. Sobol, C. H. Thurber, and H. F. Wang (2024), WHOLESCALE Modeling of Hydro-Mechanical Processes at San Emidio, Nevada, U.S. on Time Scales of Days, paper presented at PROCEEDINGS, 49th Workshop on Geothermal Reservoir Engineering, Stanford, California February 6-8, 2024. https://pangea.stanford.edu/ERE/pdf/IGAstandard/SGW/2024/Luo.pdf

Matlick, J. S. (1995), San Emidio Geothermal System, Empire, Nevada: GRC Field Trip ~ October 1995, Mesquite Group, Inc., Fullerton, California. https://data.nbmg.unr.edu/public/Geothermal/GreyLiterature/Matlick_SanEmidioGeoSystem_1995.pdf

Moeck, I. (2011), Stress Inversion and 2D fault stress modeling San Emidio: Project Report to PI Teplow, 19 pp.

Oppenheimer, D. H., P. A. Reasenberg, and R. W. Simpson (1988), Fault plane solutions for the 1984 Morgan Hill, California, Earthquake Sequence: Evidence for the state of stress on the Calaveras Fault, Journal of Geophysical Research: Solid Earth, 93, 9007-9026. https://doi.org/10.1029/JB093iB08p09007

Pitz, W., and D. Miller (2010), The TerraSAR-X Satellite, Geoscience and Remote Sensing, IEEE Transactions on, 48, 615-622. http://dx.doi.org/10.1109/TGRS.2009.2037432

Pulliam, R. J., F. Sepulveda, J. S. Thangraj, D. Quiros, J. Queen, M. Queen, and J. Iovenitti (2019), Development of a Novel, Near Real Time Approach To Geothermal Seismic Exploration And Monitoring Via Ambient Seismic Noise Interferometry, Medium: ED pp, Baylor Univ., Waco, TX (United States). https://www.osti.gov/servlets/purl/1648329

Reinisch, E. C., M. Cardiff, J. Akerley, I. Warren, and K. L. Feigl (2019), Spatio–Temporal Analysis of Deformation at San Emidio Geothermal Field, Nevada, USA Between 1992 and 2010, Remote Sensing, 11, 1935. http://dx.doi.org/10.3390/rs11161935

Rhodes, G. T., J. E. Faulds, and W. Teplow (2010), Structural Controls of the San Emidio Desert Geothermal Field, Northwestern Nevada, paper presented at Geothermal Resource Council Transactions.

Rhodes, G. T. (2011), Structural controls of the San Emidio Geothermal System, M.S. thesis, vi, 73 leaves pp, University of Nevada Reno advisor).

Rhodes, G. T., J. E. Faulds, and A. R. Ramelli (2011), Preliminary Geologic Map of the Northern Lake Range, San Emidio Geothermal Area, Washoe County, Nevada, Nevada Bureau of Mines and Geology. http://data.nbmg.unr.edu/public/freedownloads/of/of2011-11.zip

Settgast, R. R., J. A. White, B. C. Corbett, A. Vargas, C. Sherman, P. Fu, and C. Annavarapu (2018), GEOSX Simulation Framework: General multi-physics simulation framework targeting exascale computing platforms, Medium: X; OS: Any pp., Lawrence Livermore National Lab. (LLNL), Livermore, CA (United States). https://www.osti.gov/biblio/1422506

Sone, H., Z. Jin, O. Mudatsir, I. Warren, M. Folsom, and K. L. Feigl (2023), WHOLESCALE - Characterization of Conductive Fractured Zones Based on Borehole Data at San Emidio Geothermal Field, Nevada, paper presented at Stanford Geothermal Workshop. https://pangea.stanford.edu/ERE/db/GeoConf/papers/SGW/2023/Sone.pdf

Teplow, W. J., and I. Warren (2015), Finding Large Aperture Fractures in Geothermal Resource Areas Using a Three-Component Long-Offset Surface Seismic Survey, PSInSAR and Kinematic Structural Analysis, Medium: ED; Size: 52 p. pp, US Geothermal, Inc., Boise, ID (United States). https://doi.org/10.2172/1213113

Torres, R., P. Snoeij, D. Geudtner, D. Bibby, M. Davidson, E. Attema, P. Potin, B. Rommen, N. Floury, M. Brown, I. N. Traver, P. Deghaye, B. Duesmann, B. Rosich, N. Miranda, C. Bruno, M. L'Abbate, R. Croci, A. Pietropaolo, M. Huchler, and F. Rostan (2012), GMES Sentinel-1 mission, Remote Sensing of Environment, 120, 9-24. http://dx.doi.org/10.1016/j.rse.2011.05.028

UNR (2014), Slip and Dilation Tendency Analysis of the San Emidio Geothermal Area [data set]. https://gdr.openei.org/submissions/371

Vavryčuk, V. (2014), Iterative joint inversion for stress and fault orientations from focal mechanisms, Geophysical Journal International, 199, 69-77. https://doi.org/10.1093/gji/ggu224

Warren, I. (2010), Three-Component Long Offset Surface Seismic Survey Data Used to Find Large Aperture Fractures in Geothermal Resources - San Emidio Geothermal Resource Area, U.S. Geothermal Inc. https://doi.org/10.15121/1422726

Warren, I., E. Gasperikova, and S. Pullammanappallil (2019), Final Phase 1 Report DE-EE0007698: A Novel Approach to Map Permeability Using Passive Seismic Emission Tomography. https://subterraseis.com/wp-content/uploads/2019/10/Doc1.pdf